energy&fuels

Article

Size distribution and fractal characteristics of coal pores through nuclear magnetic resonance cryoporometry

Tingting Yin, Dameng Liu, Yidong Cai, Yingfang Zhou, and Yanbin Yao

Energy Fuels, **Just Accepted Manuscript** • DOI: 10.1021/acs.energyfuels.7b00389 • Publication Date (Web): 11 Jul 2017

Just Accepted

ACS Publications

Energy & Fuels is published by the American Chemical Society. 1155 Sixteenth Street N.W., Washington, DC 20036

Size distribution and fractal characteristics of coal pores through nuclear magnetic resonance cryoporometry

Tingting Yin[a], Dameng Liu[a]*, Yidong Cai[a], Yingfang Zhou[b], Yanbin Yao[a]

[a] School of Energy Resources, China University of Geosciences, Beijing 100083, China

[b] School of Engineering, Fraser Noble Building, King's College, University of Aberdeen, AB24 3UE Aberdeen, UK

Abstract: Characterization of the coal pore structure plays a critical role in the adsorption and flow of coalbed methane (CBM) during CBM exploitation. The accuracy of conventional techniques is relatively low, especially for micropores. Nuclear magnetic resonance cryoporometry (NMRC), as a new technique that is used to detect the pore structure of porous media, has been applied to many fields. However, it is rarely used for CBM reservoirs. In this study, the pore size distribution (PSD) and fractal characteristics of semianthracites and anthracites are investigated through NMRC, routine NMR and low-temperature nitrogen adsorption methods. The results show that the PSD obtained from NMRC is divided into three types, which are mainly affected by the metamorphic degree of the selected coals (coal rank). Type I PSD from NMRC shares a high consistency with that yielded by NMR. The comparison between PSD from NMRC and NMR shows that the NMR method yields a higher pore volume for adsorption pores than that of NMRC due to the presence of skeleton information and paramagnetic impurities. The fractal result of coal pores from NMRC indicates that the transition pores and mesopores are more complex than the micropores. Moreover, the results from NMRC represent a more accurate pore

structure for the same coal sample compared with NMR. The relationships between pore volume, permeability, Langmuir volume and pore fractals has also been established, which proves that, as a new method, NMRC is of great significance in characterizing the petrophysical properties of CBM reservoirs.

Key words: Nuclear magnetic resonance cryoporometry (NMRC); pores; fractal characterization; permeability; Langmuir volume

1. Introduction

Coalbed methane (CBM) reservoirs are a type of important heterogeneous reservoir within which the pore structure has an important role in controlling gas adsorption and flow. Common methods for detecting pores of large diameter (>500 nm) include the use of a scanning electron microscope [1], CT scanning technique [2] and mercury intrusion porosity (MIP) [3]. Moreover, compared with conventional reservoirs, including those composed of sandstones and carbonates, the pores in CBM reservoirs are relatively small and are characterized by strong compressibility [4]. Therefore, the determination of the pore structure of micropores using conventional experimental methods, such as MIP and low-temperature nitrogen adsorption methods, is greatly limited by the accuracy of these techniques [5, 6]. In recent decades, new methods, such as nuclear magnetic resonance (NMR) [7], small angle neutron scattering (SANS), ultra-small angle neutron scattering (USANS) [8] and small angle X-ray scattering (SAXS) [9], have been applied to unconventional tight reservoirs, including shale gas and CBM reservoirs. These techniques are characterized by accuracies that

are higher than those of conventional methods, especially for closed pores of < 2 nm. Nuclear magnetic resonance cryoporometry (NMRC) is a new method that can translate temperature information into pore structure information. Therefore, the pore size distribution (PSD) of heterogeneous porous materials can be accurately investigated. To-date, this method has been widely applied to many materials, such as porous silica, soil, ceramics, cement and concrete, to study the aspects of pore structure, pore morphology, moisture content, pore size imaging and interaction between water and hydrophilic/hydrophobic surfaces [10-15]. As for coal reservoirs, previous research [16] studied pre-drying on the porous structure of water-swollen coals by controlling the temperature changes and recording the variation of different phase moistures in water-saturated coals. The freezing point distribution (FPD) for pore condensed water can be determined by NMR, which can be converted into PSD information by employing a cylindrical-shaped pore model. Another study [17] proved that pore width will be reduced with an increase in water content. Although NMRC technology has been widely used in many materials, it is rarely used to examine the pore structure of CBM reservoirs. To study the feasibility of NMRC toward quantification of the pore structure of CBM reservoirs, firstly, NMRC was adopted to investigate the PSD, pore volume and pore fractals of coal samples. Subsequently, the results from NMRC and NMR were comparatively studied, and the accuracy of NMRC was systemically examined. Finally, the effects of pores on the permeability and adsorption of the selected coals were evaluated.

2. Sampling and experiments

Thirteen coal samples were collected from the no.8 and no.15 seams of the Yangquan and Shouyang blocks in the northeastern Qinshui Basin, which is one of the largest anthracite production bases in China. These two blocks are also rich in CBM resources, which are present at high concentrations [18]. Vitrinite reflectance ($R_{o,m}$), coal composition, proximate analysis, isothermal adsorption test, NMR and NMRC experiments were conducted. The vitrinite reflectance and coal composition were determined on a Laborlxe 12 POL microscope with a MPS 60 photo system manufactured by Leitz Company of Germany. Proximate analyses were performed on a 5E-MACⅢ infrared rapid coal analyzer at the China University of Geosciences in Beijing. The isothermal adsorption tests were performed on a TerraTek-300 isothermal adsorption instrument at the Shanxi Institute of Geology and Mineral Resources.

The process for collecting NMR measurements was implemented as follows. First, the samples were dried at 80 ℃ for 24 h. According to thermal evolution history analysis[19], coals with $R_{o,m}$ greater than 2 generally experienced a temperature above 130 ℃. Therefore, the drying process can be ensured no damage to the structure. Then, vacuuming and pressure saturation of the samples was conducted. Second, a T_2 spectrum analysis test was conducted with a MacroMR12-150-H-1 rig to obtain the PSD. Finally, samples were centrifuged for 4 hours; then the two previous steps were repeated. According to the changes of the T_2 spectrum before and after water centrifugation, the movable fluid porosity and permeability were acquired via the Coates Model.

NMRC measurements were performed by using a NMRC12-010V spectrum analyzer (Fig. 1) with a main frequency of 11.053 MHz. First, the pre-treatment process was conducted as the above NMR experiments. Second, the samples of saturated water were placed into the sample slot. Meanwhile, the cold trough was cooled to -60 ℃. Then, the sample was cooled to within the preset temperature range of -30 to 0.2 ℃. The sample slot was supplied with a magnetic field, which was provided with electromagnetic waves by a radio frequency cabinet. Based on the emission and acquisition of the signal value at each temperature point, the pore volume and fractals of different pores were calculated. According to an alcohol test (Fig. 2), the signal intensity at each temperature point basically remained stable after 10 minutes, with fluctuation range lower than 5‰ of the total value, which is caused by background signal and can be ignored. Therefore, the samples were kept for 10 minutes at each temperature point.

3. Basic theory

3.1. Basics of NMRC experiment

The basic principle of NMRC follows the relationship between the pore size and phase transition temperatures for probe materials confined in pores [11] by relying on the Gibbs-Thomson thermodynamic equation [20]:

$$\Delta T_m = T_m(r) - T_m^{\infty} = -\frac{4\delta_{sl}T_m^{\infty}}{r\Delta H_f \rho_s} \quad (1)$$

where T_m^{∞} is the melting point of bulk crystal; r is the pore size; $T_m(r)$ is the melting point of a crystal with a diameter of r; δ_{sl} is the surface energy of the crystal and liquid interface; ΔH_f is the melting enthalpy of the macroscopic substances; and

ρ_s is the solid density. The negative sign indicates that the melting point of the substance within the pore is lower than the bulk melting point. The physical parameters can be regarded as constants. Thus, equation (1) can be substituted as follows:

$$\Delta T_m = -\frac{K_{GT}}{r} \quad (2)$$

where K_{GT} is a constant related to the thermodynamic properties of the probe. Based on previous study [21], K_{GT} ranges from 45 to 57 (nm·K) for coal samples and here was set at an average value of 50 (nm·K). The increase of the liquid signal with an increasing temperature can be used to reflect the accumulation of the pore volume on a large scale, as shown in Fig.3.

3.2. Calibration of NMRC signal intensity

The effects of temperature variation on NMRC signal intensity mainly includes two aspects. First, temperature variation influences the distribution of Zeeman level, which can be calibrated by the following equation [22]:

$$SI_K T_K = SI_S T_S \quad (3)$$

where T_S is calibration temperature and generally set to 0 ℃; SI_S is the signal intensity corresponding to T_S.

Second, theoretical results show that the temperature has a linear relationship with the coil resistivity in a certain temperature range, with the following expression [22]:

$$\rho(T) = \alpha + \beta \cdot T \quad (4)$$

where ρ is resistivity; α, β are thermal coefficients of the probe coil.

Signal intensity is inversely proportional to resistivity, which can be calibrated by the

following equation [22]:

$$SI_K(\alpha + \beta \cdot T_K) = SI_S(\alpha + \beta \cdot T_S) \quad (5)$$

Considering the impact of temperature on these two factors, the calibration equation could be derived:

$$SI_S = SI_K \frac{T_K(\alpha+\beta \cdot T_K)}{T_S(\alpha+\beta \cdot T_S)} = SI_K \frac{T_K(\lambda+T_K)}{T_S(\lambda+T_S)} \quad (6)$$

where $\lambda = \alpha/\beta$. The signal intensity before and after calibration are shown in Fig. 4. And therefore the NMRC results can be ensured to reflect pore structure without the influence of temperature variation.

3. 3. Fractal theory

3.3. 1. NMRC's fractal theory

According to fractal geometry theory [12], the pore size distribution is derived as follows:

$$Sv = (\frac{r}{r_{max}})^{3-D} \quad (7)$$

where r_{max} is the maximum pore diameter; Sv is the percentage of pore accumulating volume in the total pore volume when the pore size is less than r; and D is the pore fractal dimension.

According to Equation (2), the following equation can be derived:

$$\Delta T_{m\,max} = -\frac{K_{GT}}{r_{max}} \quad (8)$$

Substituting equations (2) and (8) into (7):

$$Sv = (\frac{\Delta T_{m\,max}}{\Delta T_m})^{3-D} \quad (9)$$

Using logarithms for equation (9), this can be revised as:

$$\lg(Sv) = (D-3)\lg(-\Delta T_m) + (3-D)\lg(-\Delta T_{m\,max}) \quad (10)$$

Through $\lg(Sv)$ and $\lg(-\Delta T_m)$, the slope K can be acquired. Then,

$$D = K + 3 \tag{11}$$

3.3.2. NMR's fractal theory

Based on fractal geometry, the approximate fractal geometry equation [23] corresponding to the NMR T_2 spectrum can be derived as:

$$Sv = \left(\frac{T_{2\,max}}{T_2}\right)^{D-3} \tag{12}$$

Using logarithms for equation (12):

$$\lg(S_V) = (3 - D)\lg(T_2) + (D - 3)\lg(T_{2\,max}) \tag{13}$$

Based on the linear relationship between $\lg(Sv)$ and $\lg(T_2)$, the fractals of coal pore structure can be calculated.

After centrifugation, the T_2 spectrum is redrawn, and the difference in the signal before and after centrifugation reflects the volume of the movable fluid [24]. Replacing the cumulative pore volume fraction Sv in equation (9) with the cumulative active pore volume fraction Sv', equation (13) becomes:

$$\lg\left(S_v^{'}\right) = (3 - D_M)\lg(T_2) + (D_M - 3)\lg(T_{2\,max}) \tag{14}$$

Therefore, the fractals of the movable fluid pores in coal can be analyzed by considering D_M.

4. Results and discussion

4.1. Coal basic information

The results of $R_{o,m}$ and the coal composition, as well as of the proximate analyses, are summarized in Table 1. The $R_{o,m}$ of coal samples ranges from 2.22%-3.35% and the coal rank is given priority for semianthracites and anthracites. The macerals are

mainly composed of vitrinite, while exinite cannot be found under the microscope due to the high grade of metamorphism. Proximate analysis indicates that the contents of the moisture, ash, volatile material and fixed carbon range from 0.88 to 1.63%, 8.78 to 13.41%, 12.43 to 18.38%, and 70.09 to 74.31%, respectively.

4.2. Pore structure by NMR and NMRC

4.2.1. Pore size distribution

NMRC acquires the PSD of coal by detecting the liquid probe content in the porosity with a gradually increasing temperature. Based on Hodot's pore classification [25], the pores can be divided into micropores (< 10 nm in diameter), transition pores (10-100 nm in diameter), mesopores (100-1000 nm in diameter) and macropores (> 1000 nm in diameter), in which micropores constitute CBM adsorption area, transition pores constitute the capillary condensation and diffusion area, mesopores and macropores form the zone of CBM slow and rough laminar flow, respectively. The pore size that the NMRC technique measured ranges from 1.6 to 500 nm. Therefore, NMRC can detect the pore structure of micropores, transition pores and a limited range of mesopores, which is much less than the scale measured by NMR. This limitation in the detection scale is related to the probe material (water) that in pores with a diameter > 500 nm is in the free water state. The melting point reaches a constant of 0℃, making it impossible to increase the liquid volume through a further rise in temperature. On the other hand, there are only a few water molecules in nanoscale pores with pore sizes < 1.6 nm. Therefore, there is almost no difference between ice and water due to a water molecule diameter of 0.4 nm. In other words, no

phase transition can be found in pores that have a diameter < 1.6 nm. Moreover, ultramicropores (< 1.6 nm) require especially low temperatures for NMRC, and therefore, the NMRC can only accurately measure PSD information for pores with diameters > 1.6 nm.

The PSD curves acquired from NMRC are mainly divided into three types (Fig. 5). Type I shows a bimodal distribution. The pore size of the first peak ranges from 2 to 10 nm, with a peak value larger than 0.02 cm^3/g. The second peak is mainly distributed between 30 to 500 nm, and the peak value is relatively low. Type I corresponds to coal samples with $R_{o,m}$ values ranging between 2.2% and 2.5%. Type II has a peak value that is obviously higher than that of type I, which only retains the second half of the first peak. The corresponding $R_{o,m}$ value is between 2.5% and 3.1%. The PSD curve of type III is characterized by relatively low values, with a peak value in the vicinity of 0.01 cm^3/g, corresponding to $R_{o,m}$ estimates of 3.1% to 3.35%. According to previous research [26] (shown in Fig. 6), for high rank coal and with a change in the $R_{o,m}$ estimates, the porosity experienced a gradual increase and then declined. Considering a value of approximately 2.3% as the boundary, and for $R_{o,m}$ values lower than 2.3%, almost all oxygen-containing functional groups fall off, the aromatic rings of coal gradually increase, and the order of arrangement improves. After $R_{o,m}$ reaches the 2.3% boundary, the aromatic structure of coal is further enhanced and the whole porosity demonstrates a decreasing trend. Therefore, for the coal samples studied, the PSD curves show a transition from type I to type II, with an increase of $R_{o,m}$ from 2.2% to 2.5%. At this stage, the micropore and transition pore

volumes increase to various degrees, causing the PSD curves to shift toward the left, with an increase in the peak value. The boundary of this study is greater than 2.3%. After exceeding the boundary, the volume of micropores and transition pores begins to reduce and the curves transfer from type II to type III.

Fig. 7 illustrates the comparison of PSD curves from NMRC and NMR. In terms of the distribution pattern, the type I curve of NMRC shares a high consistency with that of NMR. Meanwhile, the consistencies observed for types Ⅱ and Ⅲ are relatively poor, which may be caused by the different ranges of vitrinite reflectance. The PSD from the T_2 spectrum of NMR shows the typical three peaks of adsorption pores, seepage pores and fractures [27], while that from NMRC only reveals two peaks in the diameter range of 1.6-500 nm and is absent from the fracture peak. Additionally, there is a slight difference in the pore volume of the seepage pore peak between NMR and NMRC. However, for the peak of adsorption pores, the NMR method yields a significantly higher pore volume than NMRC. The reason for this phenomenon may be related to the skeleton information. Because H in the solid skeleton has a shorter relaxation time, there will be an increase in the amount of signal for small diameter portions. The presence of sodium, potassium, iron and other paramagnetic impurities will also shorten the relaxation time [28-30], which ultimately increases the proportion of micropores and transition pores. At this point, NMRC screens the background value signal at the initial temperature of -30 °C, excluding interference factors, such as the skeleton information [10, 11], and therefore, the pore volume in adsorption pores from NMRC is smaller than that from NMR. Moreover, there are

relatively steep as well as smooth pore volume changes in the peaks of adsorption pores observed for NMR, while the curves for NMRC are sensitive, indicating a limited resolution for the NMR method [31]. In summary, the PSD curves from NMRC are more accurate.

Fig. 8 demonstrates the pore volume ratio at different pore sizes measured by NMRC. Pore sizes below 500 nm are dominated by micropores and transition pores. Nearly 80% of the samples are characterized by micropore volumes distributed between 40%-70% of the total volume; the transition pore volumes, which are composed of secondary micropores, accommodate 25%-50% of the total pore volume; the volume of mesopores in the range of 100 nm to 500 nm is substantially scarce, as over 90% of the samples were evaluated at mesopore volumes of less than 15% of the total volume. Ultimately, this type of pore structure, which is primarily typified by dominant micropores and mesopores, can greatly improve the specific surface area of a coal reservoir, which can thus provide more adsorption sites for CBM storage. On the other hand, the pore structure of pores with diameters < 100 nm is generally complex due to poor connectivity. This requires an effective method with which to determine the complexity of the pore structure in coals, which will be elaborated below through a combination of fractal features and pore connectivity.

4.2.2. Relation between the pore volume by NMRC and low-temperature nitrogen adsorption methods

As shown in Fig.9, the pore volume obtained by NMRC is significantly greater than by low-temperature nitrogen adsorption method, with approximately an order of

magnitude difference. While with the increase of $R_{o,m}$, the variation tendency of pore volume from the two methods is basically the same (sample SY5 as an outlier). According to the contrast of the pore volume proportions in different pore sizes (Fig.10), the PSD information of NMRC turns out to be comparatively more complete and the pore volume is roundly distributed in the range of 1-500 nm, with clear peak values. However as for the curves of LP-N2GA, the pore volume is mainly concentrated in the pore sizes larger than 10 nm, and with a relatively single peak value. Since LP-N2GA method is insufficient to measure closed pores in coal [13], the NMRC method is superior in acquiring pore volume, especially for the micropores with pore size < 10 nm.

4.3. Fractal characteristics and its controlling factors

4.3.1. Fractal characteristics

The fractal dimensions obtained by NMRC (D_{NMRC}) range from 2.491-2.834, and there is an obvious inflection point in the fractal curve, thus it can be divided into two sections with pore sizes ranging from 3 to 10 nm and 10 to 500 nm (Fig. 11). Based on Hodot's pore classification, D_1 and D_2 respectively represent the fractal dimensions of micropores and transition pores, mesopores. The slope of segment D_1 is significantly smaller than that of segments D_2 and the fractal dimensions, D_1 and D_2, range from 1.66-2.83, 2.48-2.91, respectively, which indicates that the transition pores and mesopores are more complex than the micropores. As shown in Fig.12, there is a positive linear relationship between D_2 and LP-N2GA fractal dimension (D_L), which indicates that D_2 has a certain influence on pore surface roughness with pore sizes

between 10-500 nm.

The section between 1 and 3 nm is ignored for its results are inaccurate [32], which is caused by the freezing-melting hysteresis [11]; freezing-melting hysteresis occurs a state that in the process of lowering the temperature to induce freezing, the pore-confined liquid may be trapped in a metastable state, which is separated from the state of true thermodynamic equilibrium by an energy barrier. Overcoming the energy barrier is generally accomplished via two mechanisms: (1) driving the temperature to achieve the new critical point through supercooling or (2) freezing the liquid through the transfer mechanism of the propagation of the solidification front from a pore opening toward the pore interior. The rig is cooled by gas injection, which makes it difficult to reach the critical temperature of thermodynamic equilibrium. For the pore size range of 1-3 nm, the requisite temperature is lower than -30 ℃. Moreover, the bound water in pores < 3 nm is unable to connect with the frozen liquid due to poor pore connectivity. Thus, liquid in pores < 3 nm cannot be completely frozen through either of these two mechanisms [33], thus the liquid signal may be excluded because it may have been misinterpreted as a background signal before the increase in temperature, consequently resulting in erroneous data for the pore sizes under 3 nm.

The fractal dimensions of NMRC and NMR are shown in Fig. 13. Obviously, the fractal dimension of NMRC (D_{NMRC}) is larger than that of NMR (D_{NMR}). One reason for this phenomenon is neglecting the relaxation time caused by diffusion in the calculation of NMR. Relaxation time includes the body relaxation time (T_{2B}), surface relaxation time (T_{2S}) and relaxation time caused by diffusion (T_{2D}) as follows[30,32]:

$$\frac{1}{T_2} = \frac{1}{T_{2B}} + \frac{1}{T_{2S}} + \frac{1}{T_{2D}} \quad (15)$$

And T_{2D} and T_{2S} are normally ignored in the NMR calculation as follows:

$$\frac{1}{T_2} \approx \frac{1}{T_{2S}} = \rho_2(\frac{S}{V}) \quad (16)$$

While due to the significant heterogeneity of high-rank coal samples, T_2 is seriously affected by diffusion. Therefore, the calculation error may exist without even considering T_{2B} and T_{2D}. Another reason for the phenomenon is that the inversion results of routine NMR are not unique during the calculation process of the attenuation signal in the echo interval. The pore structure measured by NMR is relatively inaccurate and has a low resolution. By contrast, the NMRC technique yields small uncertainties in temperature at each small incremental step [34] and can accurately characterize the pore structure of coals with a higher resolution, the result of which is that the D_{NMRC} is larger than the D_{NMR}.

4.3.2. Effects of porosity on fractal characteristics by NMRC

Fig. 14 shows the relationships between D_{NMRC} and the volume of micropores, transition pores and mesopores. These relationships indicate that D_{NMRC} has an obvious correlation to the volume of micropores and transition pores, while there is no significant correlation between D_{NMRC} and the mesopore volume, indicating that D_{NMRC} is chiefly influenced by the heterogeneity of micropores and transition pores in high-rank coals.

There is a positive correlation between D_{NMRC} and the micropore volume (Fig. 14a), which is related to the properties of micropores, namely, a large specific surface area, poor connectivity and complex pore structure. D_{NMRC} is related to the transition pore

volume by a quadratic polynomial, including a positive correlation when D_{NMRC} < 2.62 and a negative correlation when D_{NMRC} > 2.62 (Fig. 14b). The relationship between D_{NMRC} and the transition pore volume is primarily controlled by the different stages of coalification [35]. In Fig. 15, at the first step of coalification with low values of D_{NMRC}, a positive relationship between the volume of micropores and transition pores is observed, while the second stage demonstrates a negative relationship in which high values of micropore volumes correspond to low values of transition pore volumes, and vice versa. The reason for this relationship is that when the D_{NMRC} is lower than the critical point, the degree of coalification is relatively low. In this stage, the oxygen-containing functional groups, side chain bridges and hydrogen bonds are well-developed in coals and the coal structure is relatively loose. Tectonic deformation has a significant effect on the pore structure. With the side chains and functional groups decomposing into small molecular hydrocarbons in coals, seepage pores with good connectivity and a simple porous structure may be converted into adsorption pores [1], which improves the volume of micropores and transition pores and consequently improves the density and heterogeneity. When D_{NMRC} is higher than the critical point, the transition pore volume decreases with an increase of the micropore volume. This is due to that except the volumes of mesopores and macropores decrease under conditions of high temperature and pressure during the late stage of coalification, the transition pores are also further transformed into micropores in this stage, which causes the negative correlation between the volumes of the two types of pores. Therefore, with an increasing degree of metamorphism of

coal, there is a quadratic polynomial relation between the transition pore volume and D_{NMRC}.

4.3.3. Effects of permeability on fractal characteristics by NMRC

Fig. 16 shows the correlation between fractal dimension and permeability, which is calculated by the Coates model [36, 37]. When permeability is greater than 0.05×10^{-2} mD, there is a negative correlation between the permeability and fractal dimension of the movable fluid (D_M, calculated by equation (14)) based on NMR (Fig. 16(a)), which indicates that the pore structure of the movable fluid has an influence on the seepage capacity [38-40]. The permeability increases with a decreasing heterogeneity of the movable fluid pore structure. While its correlation coefficient is low (R^2 =0.217). Moreover, in Fig. 16(b), it shows that there is a negative correlation between the permeability and D_2 with correlation coefficient much greater than that of D_M (R^2 =0.925) when permeability is greater than 0.05×10^{-2} mD. This indicates the structures of transition pores and mesopores have an influence on the permeability. And the fractal characteristics obtained from NMRC techniques can be rather more effective than NMR to evaluate the contribution of the transition pores and mesopores on the permeability of gas flow.

4.3.4. Relation between fractal characteristics and adsorption properties by NMRC

CBM is mainly adsorbed in adsorption pores and partially enriched in seepage pores in a free state, and therefore, the initial adsorption-diffusion rate of CBM is controlled by adsorption pores and seepage pores, which determine the total adsorption capacity

[41]. Fig. 17 shows the relationship between the Langmuir volume (V_L) and D_1. The V_L has a positive correlation with D_1, whereas it has no obvious correlation with D_2, indicating that micropores make the primary contribution to CBM adsorption capacity.

5. Conclusions

In this study, vitrinite reflectance and coal composition, proximate analysis, gas adsorption, permeability measurements and pore structure analysis using NMR and NMRC techniques were conducted on semianthracites and anthracites to characterize the heterogeneous features of the pore structure as well as the petrophysical properties. The following conclusions can be drawn:

1) PSD curves acquired from NMRC, are mainly divided into three types and are primarily influenced by the vitrinite reflectance. Type I is characterized by high consistency with that from NMR, while the consistency for type II is medium and that for type III is relatively poor. The comparison between the two methods indicates that the accuracy and resolution of NMRC is significantly higher than that of NMR, especially for adsorption pores.
2) The fractals measured by NMRC are divided into two sections, and fractal dimensions with various pore scales are acquired. The fractal dimensions are defined as D_1 and D_2, indicating that the surfaces of transition pores and mesopores are more complex than those of micropores. The relationship between the fractal dimensions measured by NMRC and NMR is $D_{NMRC}>D_{NMR}$.
3) NMRC fractal dimensions have an obvious relationship with the pore volume,

permeability and Langmuir volume, respectively, which indicates that it can be used as a valid parameter to evaluate the petrophysical properties of coals. Therefore, the NMRC technique can be feasibly applied as an independent method to accurately characterize the pore structure of coals.

Author information

Corresponding Author

*Tel: +86-10-82323971 (O); fax: + 86-10-82326850. E-mail: dmliu@cugb.edu.cn

Notes

The authors declare no competing financial interest.

Acknowledgments

This research was funded by the National Natural Science Foundation of China (Grant no. 41602170), the Research Program for Excellent Doctoral Dissertation Supervisor of Beijing (grant no. YB20101141501), the Key Project of Coal-based Science and Technology in Shanxi Province-CBM accumulation model and reservoir evaluation in Shanxi province (grant no. MQ2014-01) and the Fundamental Research Funds for Central Universities (grant no. 35832015136).

References

(1) Nie, B. S.; Liu, X. F.; Yang, L. L.; Meng, J. Q.; Li, X. C. *Fuel* **2015**, 158, 908-917.

(2) Yao, Y. B.; Liu, D. M. *Fuel* **2012**, 95(1), 152-158.

(3) Ritter, H. L.; Drake, L. C. *Ind. Eng. Chem. Anal.* **1945**, 17(12), 782-786.

(4) Friesen, W. I.; Ogunsola, O. I. *Fuel* **1995**, 74 (4), 604-609.

(5) Pan, Z. J.; Connell, L. D. *Int. J. Green Gas Con.* **2009**, 3(1), 77-89.

(6) Clarkson, C. R.; Freeman, M.; He, L.; Agamalian, M.; Melnichenko, Y. B.; Mastalerz, M.; Bustin, R. M.; Radlinski, A. P.; Blach, T. P. *Fuel* **2012**, 95(1), 371-385.

(7) Yao, Y. B.; Liu, D. M.; Che, Y.; Tang, D. Z.; Tang, S. H.; Huang, W. H. *Fuel* **2010**, 89(7), 1371-1380.

(8) Melnichenko, Y. B.; He, L. L.; Sakurovs, R.; Kholodenko, A. L.; Blach, T.; Mastalerz, M.; Radliński, A. P.; Cheng, G.; Mildner, D. F. R. *Fuel* **2012**, 91(1), 200-208.

(9) Okolo, G. N.; Everson, R. C.; Neomagus, H. W. J. P.; Roberts, M. J.; Sakurovs, R. *Fuel* **2015**, 141(141), 293-304.

(10) Mitchell, J.; Webber, J. B. W.; Strange, J. H. *Physics Reports* **2008**, 461(1), 1-36.

(11) Petrov, O. V.; Furó, I. *Progress in Nuclear Magnetic Resonance Spectroscopy* **2009**, 54(2), 97-122.

(12) Zhang, C. K.; Shen, J. S.; Fan, Z.; Zhang, C.; Shen, J.; Fan, Z. *Oil & Gas Geology* **2007**, 28(1), 110-115 (in Chinese with an English abstract).

(13) Guo, W.; Yao, Y. B.; Liu, D. M.; Sun, X. X.; Gao, Y. W. *Oil & Gas Geology* **2016**, 37(1), 141-148 (in Chinese with an English abstract).

(14) Gun'ko, V. M.; Turov, V. V.; Bogatyrev, V. M. *Adv. Colloid Interfac.* **2005**, 118(1-3), 125-172.

(15) Petrov, O. V.; Furó, I. *Micropor. Mesopor. Mat.* **2010**, 136(1-3), 83-91.

(16) Norinaga, K.; Hayashi, J.; Norihide, K. A.; Chiba, T. *Energy Fuels* **1999**, 13(5), 1058-1066.

(17) Hayashi, J.; Norinaga, K.; Kudo, N.; Chiaba, T. *Energy Fuels* **2001**, 15(4), 165.

(18) Hu, J. Z.; Xu, J. L.; Zhang, F. X.; Zhao, C. C.; Qin, W.; Zhu. Y. R. *Energies* **2005**, 8(7), 6881-6897.

(19) Yan, T. T.; Yao, Y. B.; Liu, D. M. *Journal of Natural Gas Science & Engineering* **2015**,

27:1367-1380.

(20) Jackson, C. L.; McKenna, G. B. *J. Chem. Phys.* **1990**, 93(12), 9002-9011.

(21) Pan, J. N.; Zhao, Y. Q.; Hou, Q. L.; Jin, Y. *Transport in Porous Media* **2015**, 107:543–54.

(22) Webber, J. B. W. Characterising porous media. *University of Kent* **2000**.

(23) Chen, Z. B.; Zhang, C. M.; Zhang, Z. S.; Ling, H. S.; Sun, B. D. *Lithologic Reservoirs* **2008**, 20(1), 105-110 (in Chinese with an English abstract).

(24) Zhou, S. D.; Liu, D. M.; Cai, Y. D.; Yao, Y. B. *Fuel* **2016**, 181, 218-226.

(25) Hodot, B. B. *Outburst of Coal and Coalbed Gas (Chinese Transl.)*; China Coal Industry Press: Beijing, **1966**; p 318.

(26) Yao, Y. B.; Liu, D. M. *Advanced Reservoir Quantitative Characterization and Comprehensive Evaluation Model of Coalbed Methane Reservoirs*; Geological Publishing House: Beijing, **2013**; p 32.

(27) Liu, D. M.; Mclean, P. A.; Curran, B.; Leader, M. *Fuel* **2012**, 95(1), 152-158.

(28) Munn, K.; Smith, D. M. *J. Colloid & Interface Science* **1987**, 119(1), 117-126.

(29) Hodgkins, M. A.; Howards, J. J. *AAPG Bull.* **1999**, 83(1), 114-127.

(30) Kenyon, W. E. *Int. J. Radiation Applications & Instrumentation. Part E. Nuclear Geophysics* **1992**, 6(2), 153-171.

(31) Zhao, Y. X.; Sun, Y. F.; Liu, S. M.; Wang, K.; Jiang, Y. D. *Fuel* **2016**, 190, 359-369.

(32) Ouyang, Z. Q; Liu, D. M.; Cai, Y. D.; Yao, Y. B. *Energy Fuels* **2016**, 30(7), 5449-5458.

(33) Webber, J. B. W. *Progress in Nuclear Magnetic Resonance Spectroscopy* **2010**, 56(1):78.

(34) Zhou, B.; Han, Q.; Yang, P. Q. *Energy Fuels* **2016**, 30(11), 9122-9131.

(35) Cai, Y. D.; Liu, D. M.; Pan, Z. J.; Liu, Z. H. *Transport in Porous Media* **2015**, 111(2),

479-497.

(36) Taicher, Z.; Coates, G.; Gitartz, Y.; Berman, L. *Magnetic Resonance Imaging* **1994**, 12(12), 285.

(37) Jerosch-Herold, M.; Thomann, H. *Magnetic Resonance Imaging* **1995**, 13(1), XII.

(38) Weniger, S.; Weniger, P.; Littke, R. *Int. J. Coal Geol.* **2016**, s 154–155, p176-192.

(39) Rushdi, A.; Gupta, R. *Fuel* **2005**, 84(5), 595–610.

(40) Jasinge, D.; Ranjith, P. G.; Choi, S. K. *Fuel* **2011**, 90(3), 1292–300.

(41) Wang, F.; Cheng, Y. P.; Lu, S. Q.; Jin, K.; Zhao, W. *Energy Fuels* **2014**, 28(9), 5729-5736.

Captions for Figures and Tables

Fig.1 Physical diagram of NMRC Spectrum Analyzer

Fig.2 Variation tendency of signal intensity in an alcohol test

Fig.3 Linear correlation between the water volume and the NMR signal intensity

Fig.4 The original and the calibrated NMR signal intensities distribution

Fig.5 Three types of PSD curves from NMRC

Fig.6 Relationship between porosity and vitrinite reflectance of coal (data from Yao and Liu, 2013)

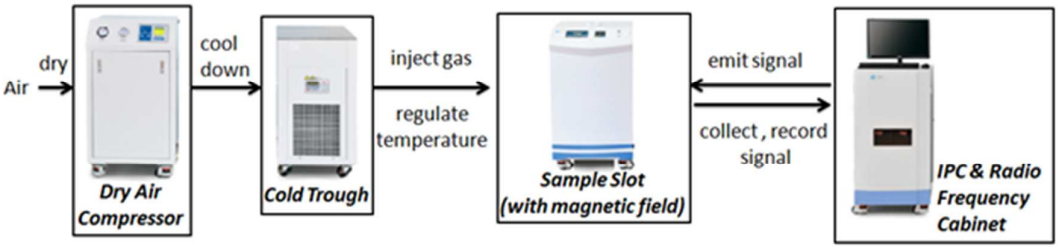
dry
Air
Dry Air
Compressor
cool
down
Cold Trough
inject gas
regulate
temperature
Sample Slot
(with magnetic field)
emit signal
collect , record
signal
IPC & Radio
Frequency
Cabinet

Fig.1

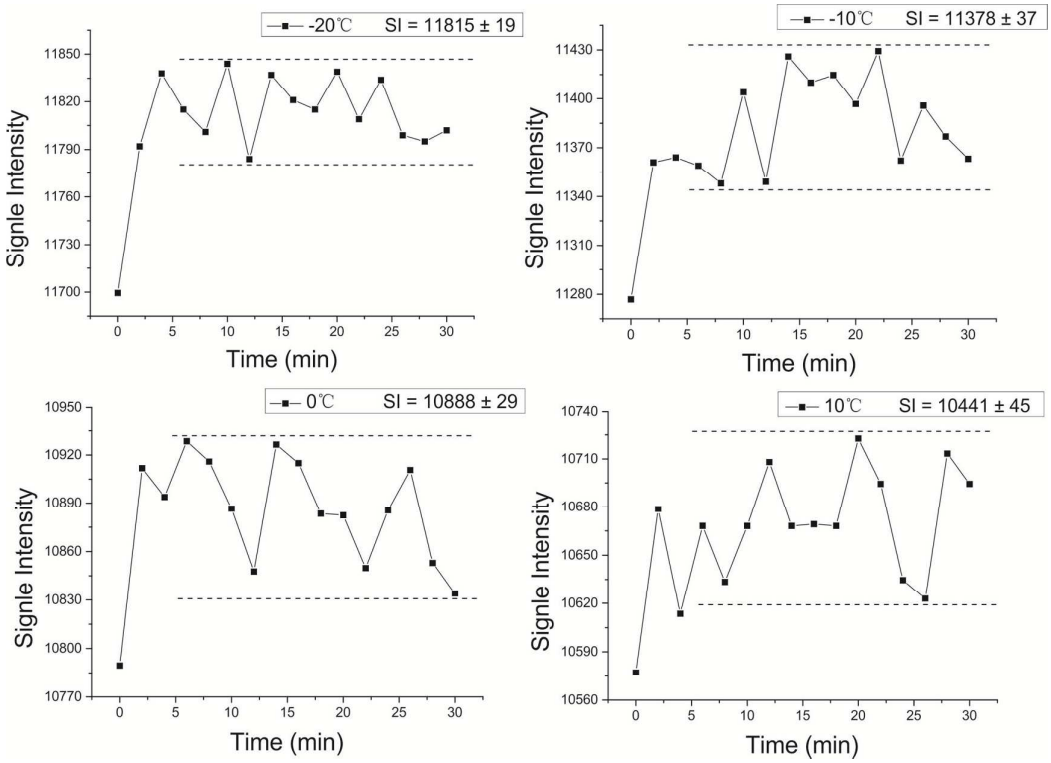
-20℃ SI = 11815 ± 19
-10℃ SI = 11378 ± 37
0℃ SI = 10888 ± 29
10℃ SI = 10441 ± 45
Signle Intensity
Time (min)

Fig.2

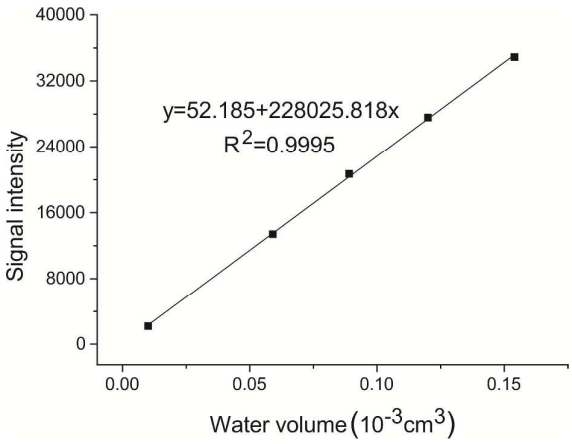
40000
32000
24000
16000
8000
0
Signal intensity
y=52.185+228025.818x
R2=0.9995
0.00
0.05
0.10
0.15
Water volume (10-3cm3)

Fig.3

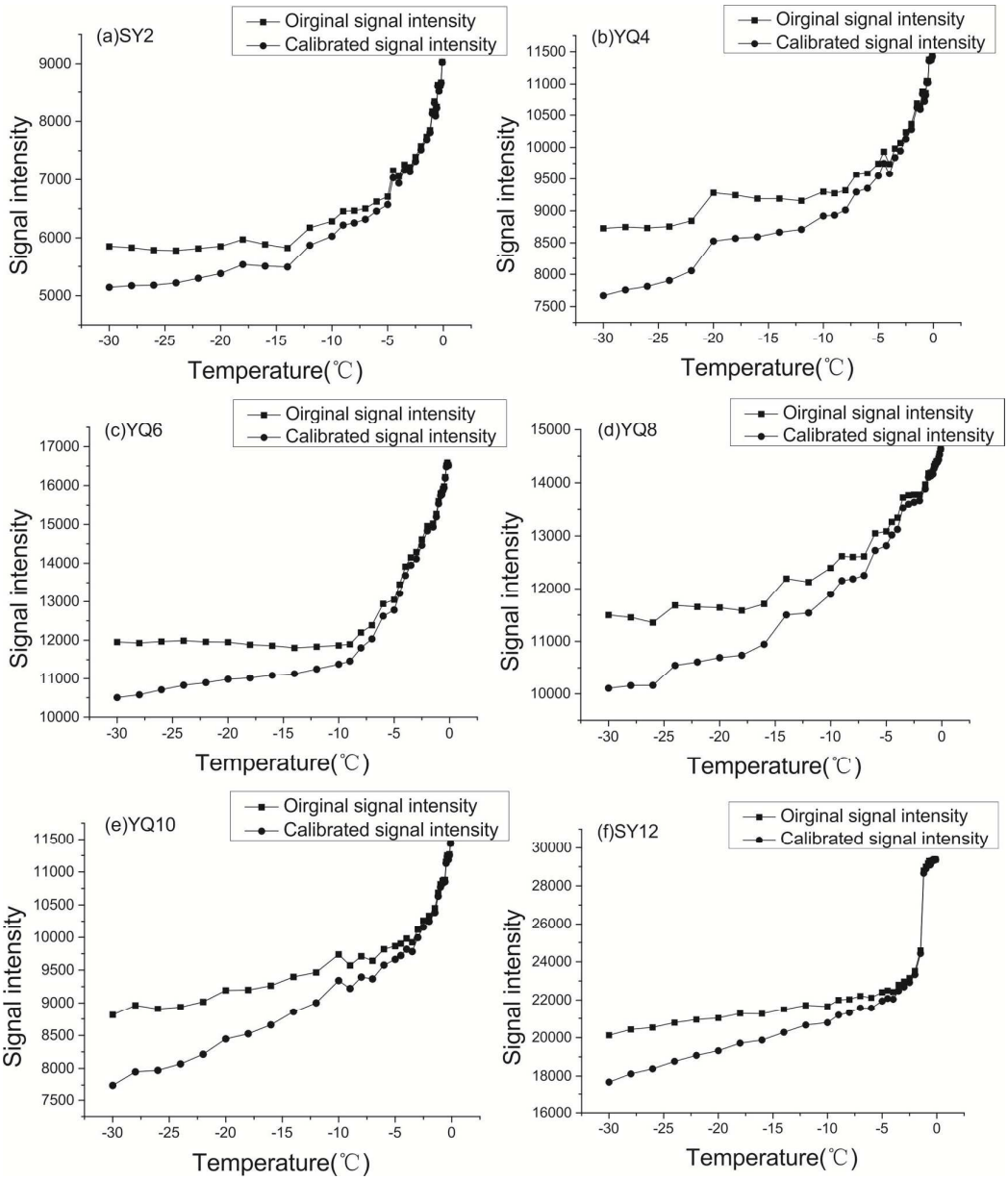
(a)SY2
Oirginal signal intensity
Calibrated signal intensity
Signal intensity
Temperature(℃)
(b)YQ4
Oirginal signal intensity
Calibrated signal intensity
Signal intensity
Temperature(℃)
(c)YQ6
Oirginal signal intensity
Calibrated signal intensity
Signal intensity
Temperature(℃)
(d)YQ8
Oirginal signal intensity
Calibrated signal intensity
Signal intensity
Temperature(℃)
(e)YQ10
Oirginal signal intensity
Calibrated signal intensity
Signal intensity
Temperature(℃)
(f)SY12
Oirginal signal intensity
Calibrated signal intensity
Signal intensity
Temperature(℃)

Fig.4

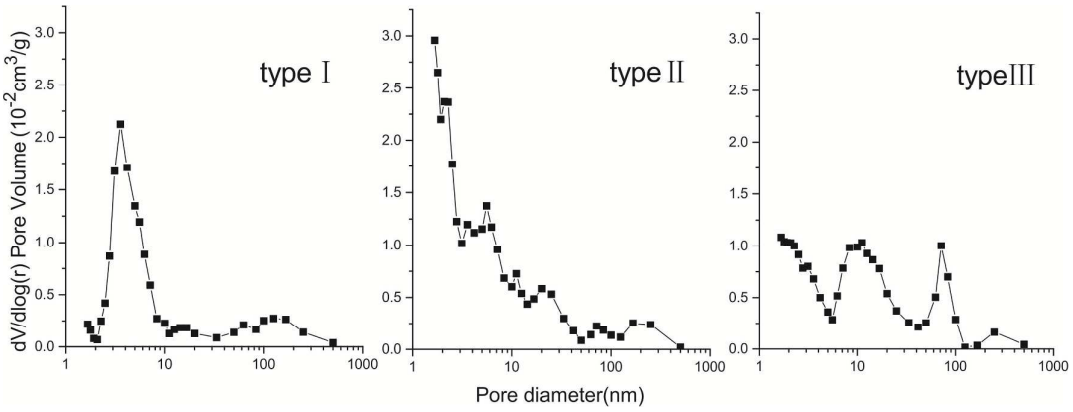
type Ⅰ
type Ⅱ
typeⅢ
dV/dlog(r) Pore Volume (10-2cm3/g)
Pore diameter(nm)
0.0
0.5
1.0
1.5
2.0
2.5
3.0
1
10
100
1000

Fig.5

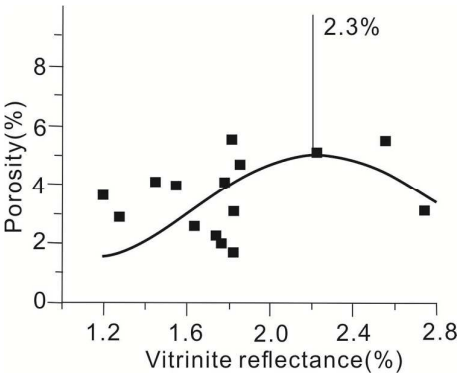

Fig.6

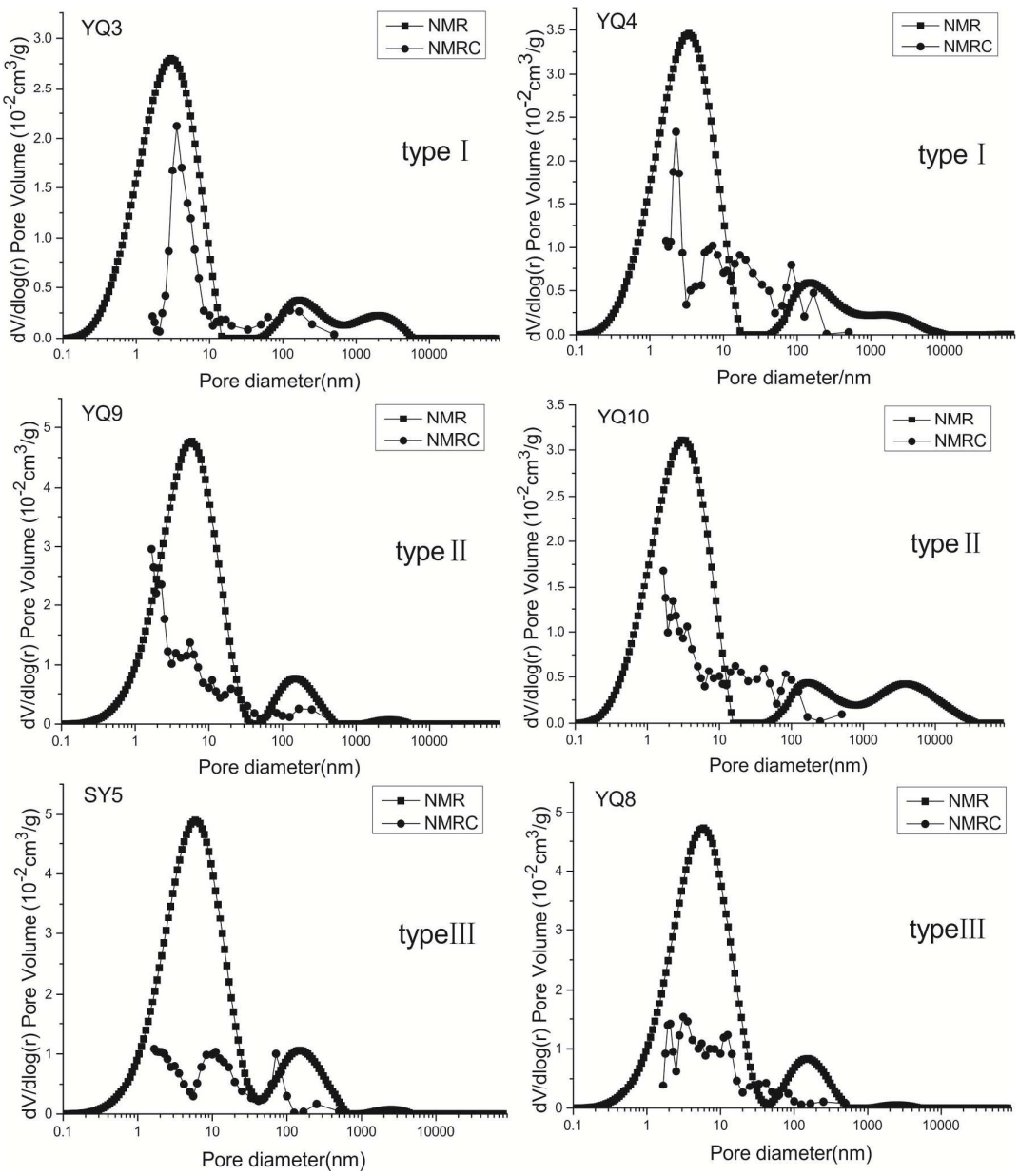
YQ3
NMR
NMRC
type Ⅰ
dV/dlog(r) Pore Volume (10^{-2}cm^3/g)
Pore diameter(nm)
YQ4
NMR
NMRC
type Ⅰ
dV/dlog(r) Pore Volume (10^{-2}cm^3/g)
Pore diameter/nm
YQ9
NMR
NMRC
type Ⅱ
dV/dlog(r) Pore Volume (10^{-2}cm^3/g)
Pore diameter(nm)
YQ10
NMR
NMRC
type Ⅱ
dV/dlog(r) Pore Volume (10^{-2}cm^3/g)
Pore diameter(nm)
SY5
NMR
NMRC
typeⅢ
dV/dlog(r) Pore Volume (10^{-2}cm^3/g)
Pore diameter(nm)
YQ8
NMR
NMRC
typeⅢ
dV/dlog(r) Pore Volume (10^{-2}cm^3/g)
Pore diameter(nm)

Fig.7

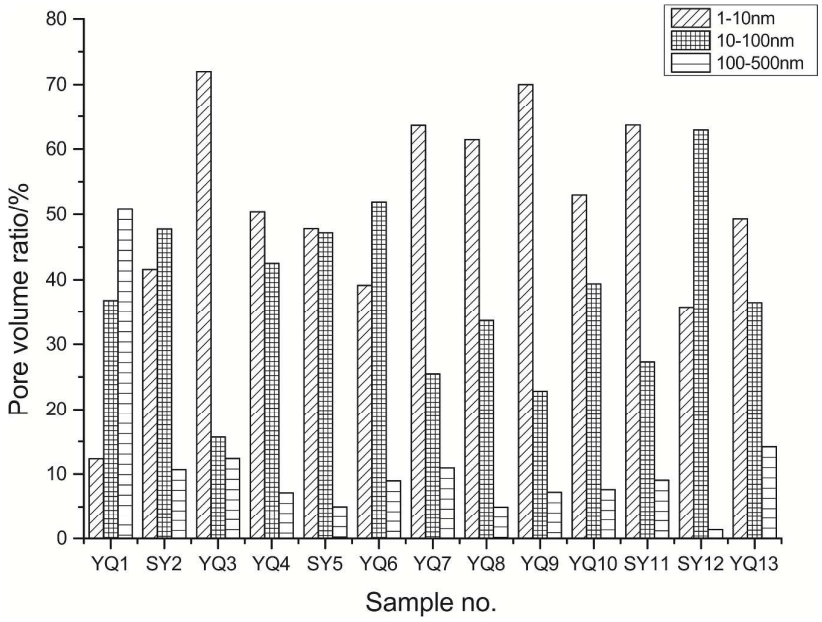
1-10nm
10-100nm
100-500nm
Pore volume ratio/%
0
10
20
30
40
50
60
70
80
YQ1
SY2
YQ3
YQ4
SY5
YQ6
YQ7
YQ8
YQ9
YQ10
SY11
SY12
YQ13
Sample no.

Fig.8

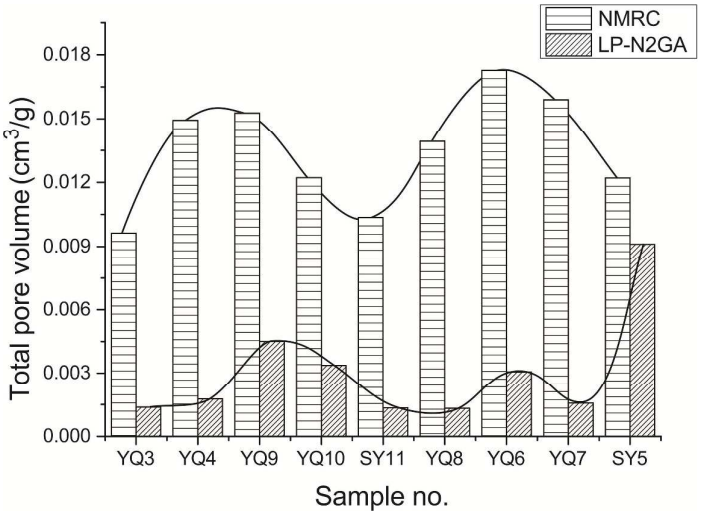
NMRC
LP-N2GA
Total pore volume (cm3/g)
0.018
0.015
0.012
0.009
0.006
0.003
0.000
YQ3
YQ4
YQ9
YQ10
SY11
YQ8
YQ6
YQ7
SY5
Sample no.

Fig.9

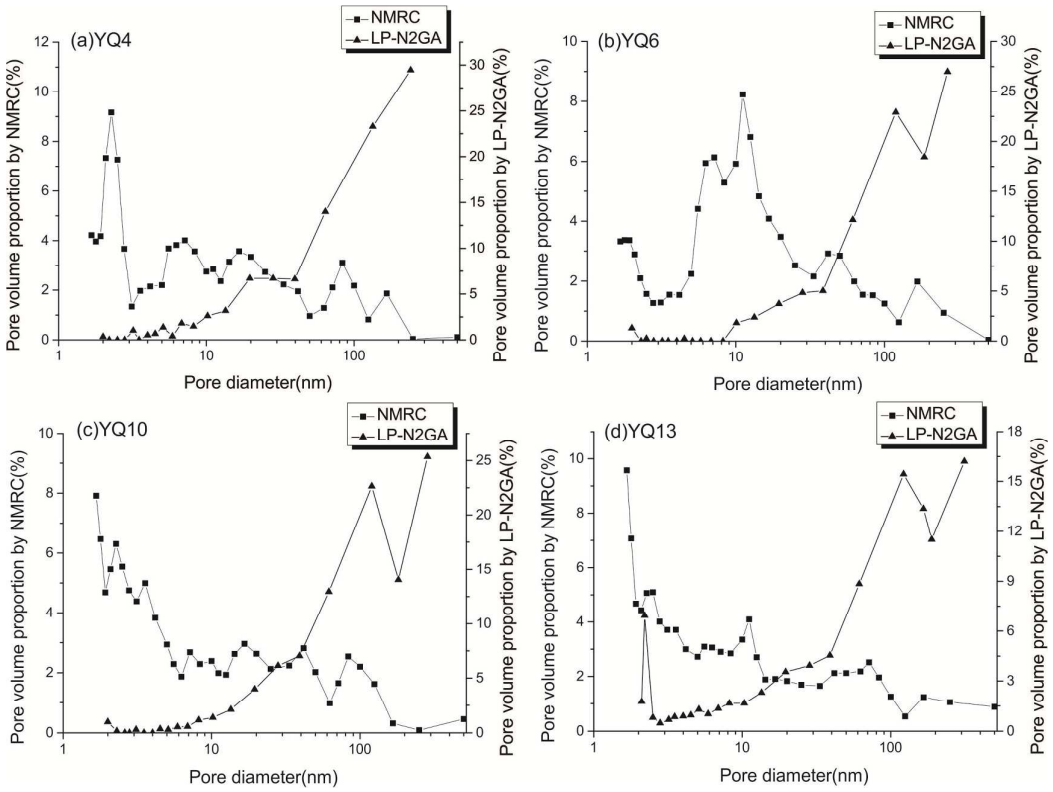
(a)YQ4
(b)YQ6
(c)YQ10
(d)YQ13
NMRC
LP-N2GA
Pore volume proportion by NMRC(%)
Pore volume proportion by LP-N2GA(%)
Pore diameter(nm)

Fig.10

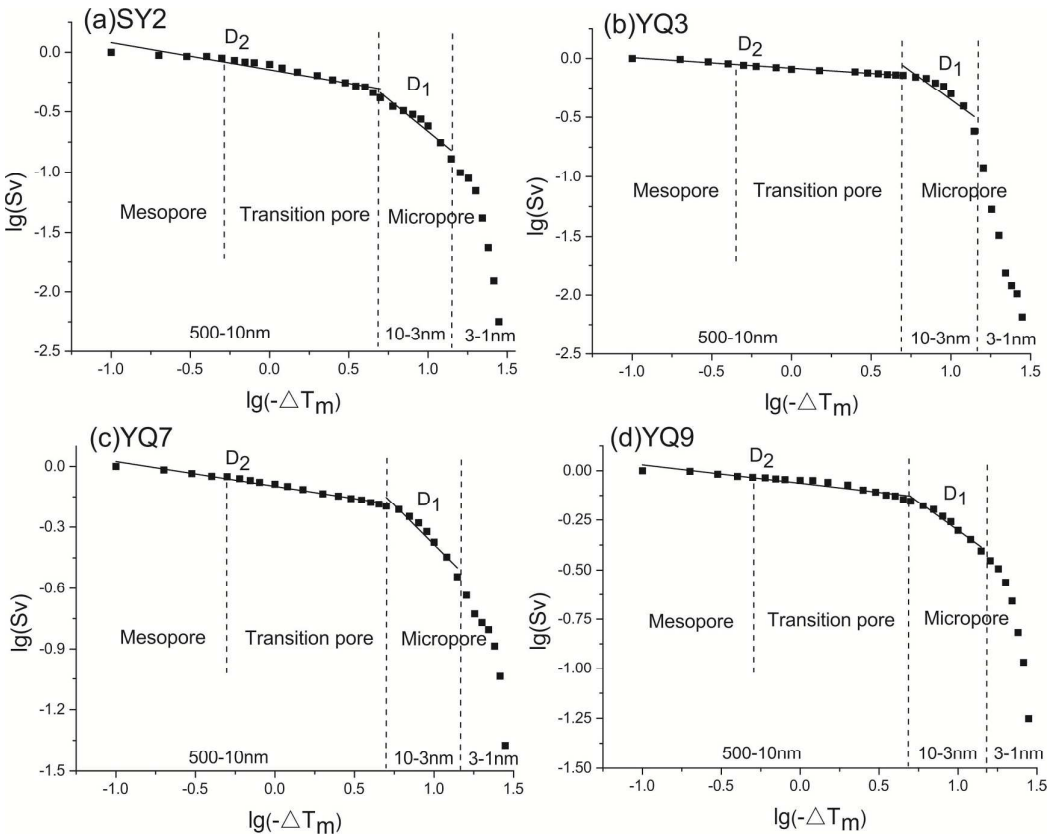
(a)SY2
D2
D1
Mesopore
Transition pore
Micropore
500-10nm
10-3nm
3-1nm
lg(Sv)
lg(-△Tm)
(b)YQ3
D2
D1
Mesopore
Transition pore
Micropore
500-10nm
10-3nm
3-1nm
lg(Sv)
lg(-△Tm)
(c)YQ7
D2
D1
Mesopore
Transition pore
Micropore
500-10nm
10-3nm
3-1nm
lg(Sv)
lg(-△Tm)
(d)YQ9
D2
D1
Mesopore
Transition pore
Micropore
500-10nm
10-3nm
3-1nm
lg(Sv)
lg(-△Tm)

Fig.11

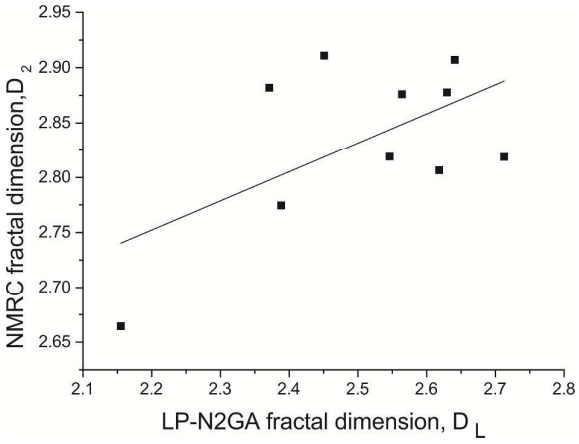
NMRC fractal dimension,D 2
LP-N2GA fractal dimension, D L
2.95
2.90
2.85
2.80
2.75
2.70
2.65
2.1
2.2
2.3
2.4
2.5
2.6
2.7
2.8

Fig.12

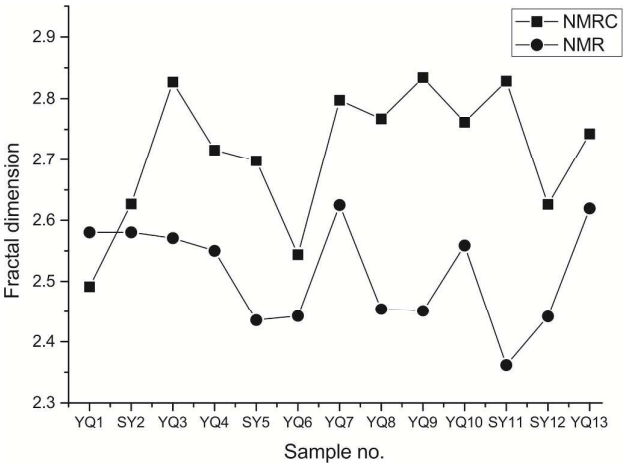
NMRC
NMR
Fractal dimension
2.9
2.8
2.7
2.6
2.5
2.4
2.3
YQ1 SY2 YQ3 YQ4 SY5 YQ6 YQ7 YQ8 YQ9 YQ10 SY11 SY12 YQ13
Sample no.

Fig.13

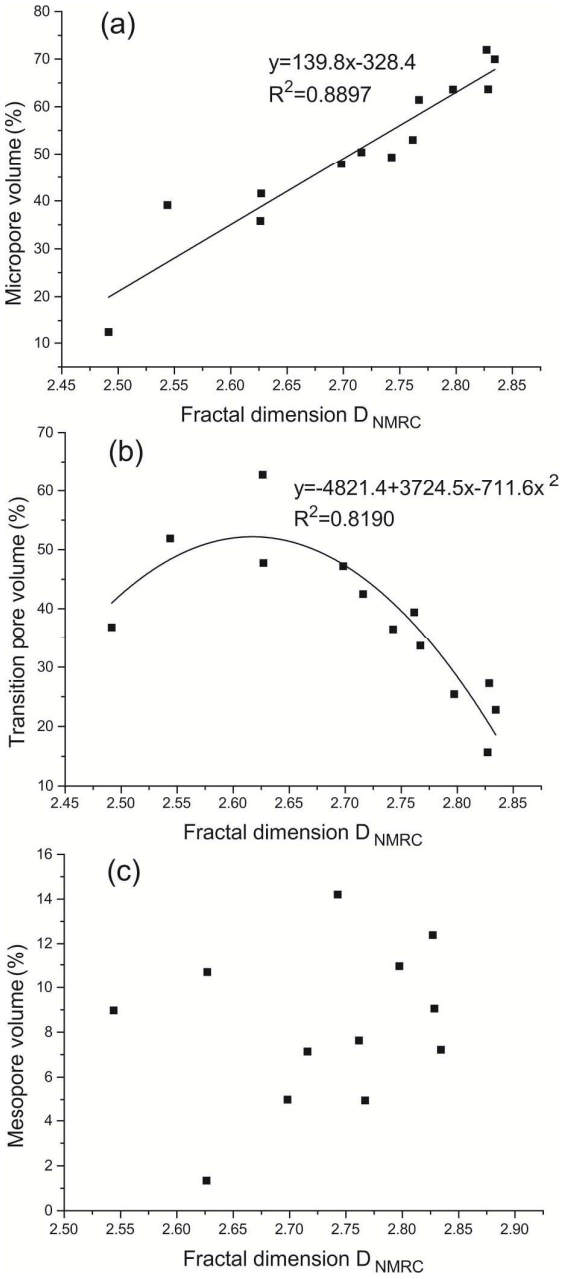
(a)
y=139.8x-328.4
R2=0.8897
Micropore volume (%)
Fractal dimension D NMRC
(b)
y=-4821.4+3724.5x-711.6x 2
R2=0.8190
Transition pore volume (%)
Fractal dimension D NMRC
(c)
Mesopore volume (%)
Fractal dimension D NMRC

Fig.14

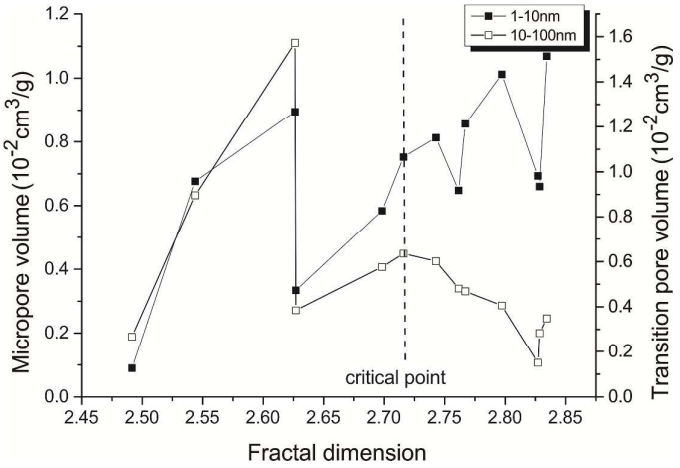
1-10nm
10-100nm
critical point
Micropore volume (10^{-2}cm^3/g)
Transition pore volume (10^{-2}cm^3/g)
Fractal dimension
0.0
0.2
0.4
0.6
0.8
1.0
1.2
1.4
1.6
2.45
2.50
2.55
2.60
2.65
2.70
2.75
2.80
2.85

Fig.15

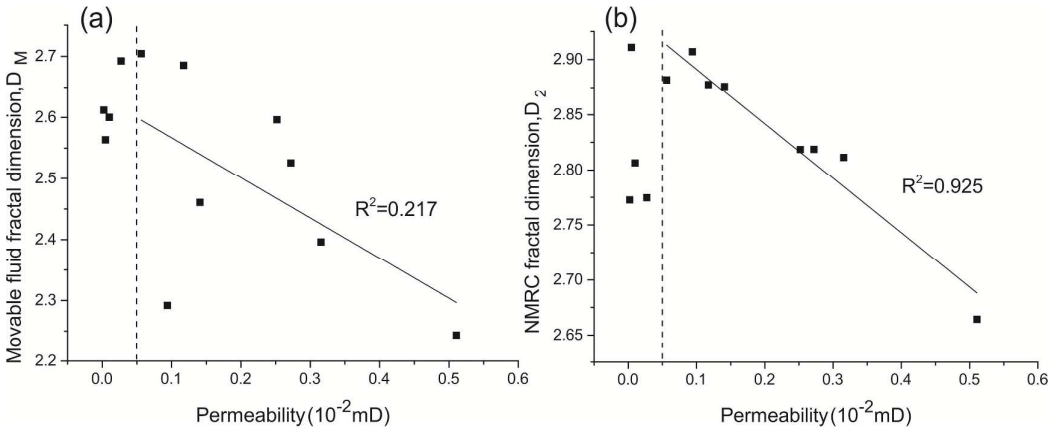
(a)
Movable fluid fractal dimension,D M
2.7
2.6
2.5
2.4
2.3
2.2
0.0
0.1
0.2
0.3
0.4
0.5
0.6
Permeability(10-2mD)
R2=0.217
(b)
NMRC fractal dimension,D 2
2.90
2.85
2.80
2.75
2.70
2.65
0.0
0.1
0.2
0.3
0.4
0.5
0.6
Permeability(10-2mD)
R2=0.925

Fig.16

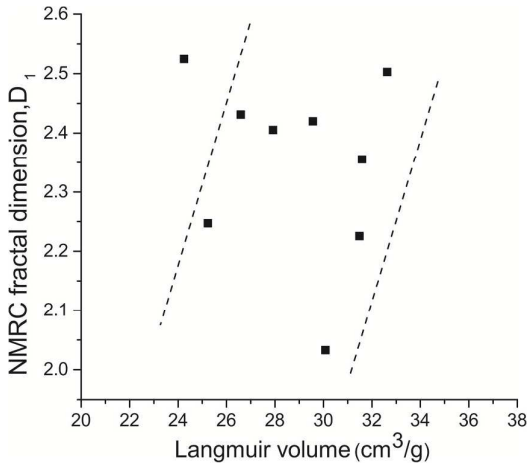
NMRC fractal dimension,D1
2.6
2.5
2.4
2.3
2.2
2.1
2.0
20
22
24
26
28
30
32
34
36
38
Langmuir volume (cm3/g)

Fig 17

Table 1

Sample no.	Vitrinite reflectance ($R_{o,max}$%)	Coal rank	Coal composition(%)			Maceral(%)		Proximate analysis(%)			
			O	B	Ot	Vitrinite	Inertinite	M	A	V	Fc
YQ1	2.440	Semianthracite	96.50	0.20	3.30	86.20	13.80	N/A	N/A	N/A	N/A
SY2	2.340	Semianthracite	91.7	0.2	8.1	84.70	15.30	0.88	12.00	17.03	70.09
YQ3	2.320	Semianthracite	95.60	0.20	4.20	87.9	12.1	0.95	10.73	17.00	71.32
YQ4	2.360	Semianthracite	97.50	0.10	2.40	89.30	10.70	N/A	N/A	N/A	N/A
SY5	3.350	Anthracite	97.10	0.40	2.50	87.40	12.60	1.62	11.50	13.37	73.51
YQ6	3.220	Anthracite	96.10	1.10	2.80	91.50	8.50	1.58	8.78	15.81	73.83
YQ7	3.250	Anthracite	96.7	1	2.3	93.9	6.1	1.61	11.55	14.61	72.23
YQ8	3.160	Anthracite	95.00	0.40	4.60	92.20	7.80	1.57	10.42	13.70	74.31
YQ9	3.000	Anthracite	93.10	1.20	5.70	93.60	6.40	1.62	9.18	18.38	70.82
YQ10	3.030	Anthracite	94.10	0.60	5.30	91.20	8.80	1.62	10.44	13.73	74.21
SY11	3.090	Anthracite	95.90	0.40	3.70	90.4	9.6	1.63	12.58	13.41	72.38
SY12	2.220	Semianthracite	92	0.3	7.7	85.30	14.70	1.07	13.41	12.43	73.09
YQ13	N/A	N/A	N/A	N/A	N/A	N/A	N/A	1.35	9.93	17.42	71.30

Note: O, B, Ot represent organic matter, brassily and other mineral composition, respectively. And M, A, V and Fc represent moisture, volatile material, ash, and fixed carbon content.

Table 2

Sample no.	D_1	R_1^2	D_2	R_2^2	D_{NMRC}	R_{NMRC}^2	D_L	R_L^2
YQ1	2.830	0.790	2.477	0.983	2.491	0.984	N/A	N/A
SY2	1.935	0.917	2.773	0.893	2.627	0.819	N/A	N/A
YQ3	2.033	0.783	2.911	0.986	2.827	0.582	2.451	0.970
YQ4	2.355	0.994	2.806	0.894	2.716	0.877	2.618	0.984
SY5	2.405	0.975	2.811	0.868	2.698	0.854	2.762	0.896
YQ6	1.661	0.981	2.775	0.820	2.544	0.763	2.388	0.943
YQ7	2.226	0.930	2.878	0.973	2.797	0.780	2.630	0.984
YQ8	2.247	0.961	2.882	0.820	2.767	0.755	2.371	0.896
YQ9	2.431	0.960	2.907	0.894	2.834	0.779	2.641	0.992
YQ10	2.503	0.927	2.819	0.905	2.762	0.906	2.546	0.972
SY11	2.525	0.938	2.876	0.944	2.828	0.879	2.564	0.970
SY12	2.529	0.957	2.664	0.785	2.626	0.897	2.155	0.967
YQ13	2.420	0.986	2.819	0.956	2.743	0.899	2.713	0.975

Note: D_1, D_2, D_{NMRC} represent the fractal dimension of micropores, transition pores and mesopores below 500 nm and the total pore space by NMRC. R_1^2, R_2^2, R_{NMRC}^2 represent the correlation coefficients, corresponding to D_1, D_2, D_{NMRC} respectively. And D_L, R_L^2 represent the fractal dimension and corresponding correlation coefficient obtained by LP-N2GA.

Table 3

Sample no.	Total pores		Movable fluid pores		Bound fluid pores	
	D_{T}	R_{T}^2	D_{M}	$\mathrm{R}_{\mathrm{M}}^2$	D_{B}	R_{B}^2
YQ1	2.829	0.970	2.303	0.816	2.584	0.473
SY2	2.580	0.440	2.612	0.486	2.578	0.442
YQ3	2.571	0.448	2.564	0.551	2.565	0.447
YQ4	2.550	0.464	2.601	0.478	2.537	0.468
SY5	2.436	0.524	2.396	0.579	2.437	0.520
YQ6	2.442	0.524	2.692	0.614	2.454	0.519
YQ7	2.625	0.431	2.685	0.606	2.321	0.545
YQ8	2.454	0.514	2.704	0.516	2.463	0.513
YQ9	2.451	0.513	2.292	0.708	2.455	0.505
YQ10	2.559	0.462	2.526	0.606	2.561	0.449
SY11	2.362	0.535	2.461	0.698	2.279	0.507
SY12	2.442	0.537	2.244	0.748	2.423	0.521
YQ13	2.619	0.432	2.596	0.790	2.243	0.523

Note: D_{T}, D_{M}, D_{B} represent the fractal dimension of total pores, movable fluid pores and bound fluid pores by NMR. And R_{T}^2, R_{M}^2, R_{B}^2 represent the correlation coefficient, corresponding to D_{T}, D_{M}, D_{B} respectively.

Table 4

Sample no.	Porosity(%)	Permeability(mD)	Langmuir volume (cm^3/g)	Langmuir pressure (MPa)
YQ1	3.87	3.30611E-05	N/A	N/A
SY2	3.64	2.1443E-05	N/A	N/A
YQ3	4.43	4.70141E-05	30.08363	1.51533
YQ4	5.57	9.95048E-05	31.59119	2.05702
SY5	7.71	0.003155595	27.91953	2.24906
YQ6	6.93	0.000271494	43.24375	2.82654
YQ7	7.77	0.001171442	31.48757	1.47757
YQ8	7.17	0.000560693	25.23	1.64
YQ9	7.03	0.000938268	26.59	2.11
YQ10	5.43	0.002720801	32.62708	1.66718
SY11	7.56	0.001408158	24.24812	1.72176
SY12	8.43	0.005107185	N/A	N/A
YQ13	7.90	0.002520479	29.56523	1.84496